

Controlling the Mobility of Ionic Liquids in the Nanopores of MOFs by Adjusting the Pore Size: From Conduction Collapse by Mutual Pore Blocking to Unhindered Ion Transport

Zejun Zhang, Modan Liu, Chun Li, Wolfgang Wenzel, and Lars Heinke*

Ionic liquids (ILs) in nanoporous confinement are the core of many supercapacitors and batteries, where the mobility of the nanoconfined ILs is crucial. Here, by combining experiments based on impedance spectroscopy with molecular dynamics simulations, the mobility of a prototype IL in the nanopores of an isoreticular metal-organic framework (MOF)-series with different pore sizes is explored, where an external electric field is applied. It has been found that the conduction behavior changes tremendously depend on the pore size. For small-pore apertures, the IL cations and anions cannot pass the pore window simultaneously, causing the ions to mutually block the pores. This results in a strong concentration dependence of the ionic conduction, where the conduction drops by two orders of magnitude when filling the pores. For large-pore MOFs, the mutual hindrance of the ions in the pores is small, causing only a small concentration dependence. The cutoff between the large-pore and small-pore behavior is approximately the size of a cation-anion-dimer and increasing the pore diameter by only 0.2 nm changes the conduction behavior fundamentally. This study shows that the pore aperture size has a substantial effect on the mobility of ions in nanoporous confinement and has to be carefully optimized for realizing highly-mobile nanoconfined ILs.

adjustable physical and chemical properties, ILs-based electrolytes are promising candidates for replacing conventional electrolytes.^[2] In most applications, such as in batteries and supercapacitors, ILs are embedded in nanoporous materials.^[3] It was found that the physicochemical properties, including the melting point, glass transition temperature, and local structure, are strongly affected by the confinement in the nanopores.^[4] A strong effect of the pore size of (amorphous) nanoporous carbon on the capacitance was also found.^[5] In addition to the astonishing insights into the static properties, theoretical calculations predicted staggering dynamic properties of ILs in the nanoconfinement of the slit pores.^[6] The dynamic aspects, which are crucial for the applications such as the charging and discharging processes of supercapacitors and batteries, have hardly been experimentally explored to date.

Metal-organic frameworks (MOFs) are a novel class of nanoporous, crystalline materials with regular, well-defined micropores.^[7] The MOF structures are tunable and their chemical functionality can be controlled by the choice of the MOF components, which are the linker molecules and the metal nodes. Due to their unique properties, MOFs have a great potential as host materials for ILs in composite electrolytes.^[3c] It is shown that the IL-filled MOFs can improve the electrochemical properties, including an enhancement of the interface wettability and an increase of the ionic conductivity in lithium batteries.^[8] Conducting MOFs filled with IL also show superior performance as supercapacitors.^[9] In these applications, the ionic conductivity of the IL electrolyte in the MOF pores is a key feature. The conductivity of the material is usually explored by using electrochemical impedance spectroscopy (EIS), where the sample is either in the form of pellets between 2 planar electrodes or as a thin film on solid substrates with deposited electrodes.^[8a,10] In previous studies, we used dense MOF thin films on a solid substrate with deposited electrodes, where excess IL can be washed off and only the conduction of the ions in the MOF pores is measured.^[10,11] In the prototype MOF-structure HKUST-1, a mutual pore blockage was found at high IL loadings, suppressing the ionic mobility and tremendously decreasing the conductivity.^[11a] In the presence of lithium ions, the IL-pore-blockage and conduction collapse is attenuated by

1. Introduction

Ionic liquids (ILs) are organic salts with melting points below room temperature.^[1] Owing to their exclusive properties, such as negligible vapor pressure, nonflammability, excellent thermal stability, high ionic conductivity, and to some extent

Z. Zhang, C. Li, L. Heinke
Institute of Functional Interfaces (IFG)
Karlsruhe Institute of Technology (KIT)
Hermann-von-Helmholtz-Platz 1
76344, Eggenstein-Leopoldshafen, Germany
E-mail: Lars.Heinke@KIT.edu

M. Liu, W. Wenzel
Institute of Nanotechnology (INT)
Karlsruhe Institute of Technology (KIT)
Hermann-von-Helmholtz-Platz 1
76344, Eggenstein-Leopoldshafen, Germany

 The ORCID identification number(s) for the author(s) of this article can be found under <https://doi.org/10.1002/smll.202200602>.

© 2022 The Authors. Small published by Wiley-VCH GmbH. This is an open access article under the terms of the Creative Commons Attribution-NonCommercial License, which permits use, distribution and reproduction in any medium, provided the original work is properly cited and is not used for commercial purposes.

DOI: 10.1002/smll.202200602

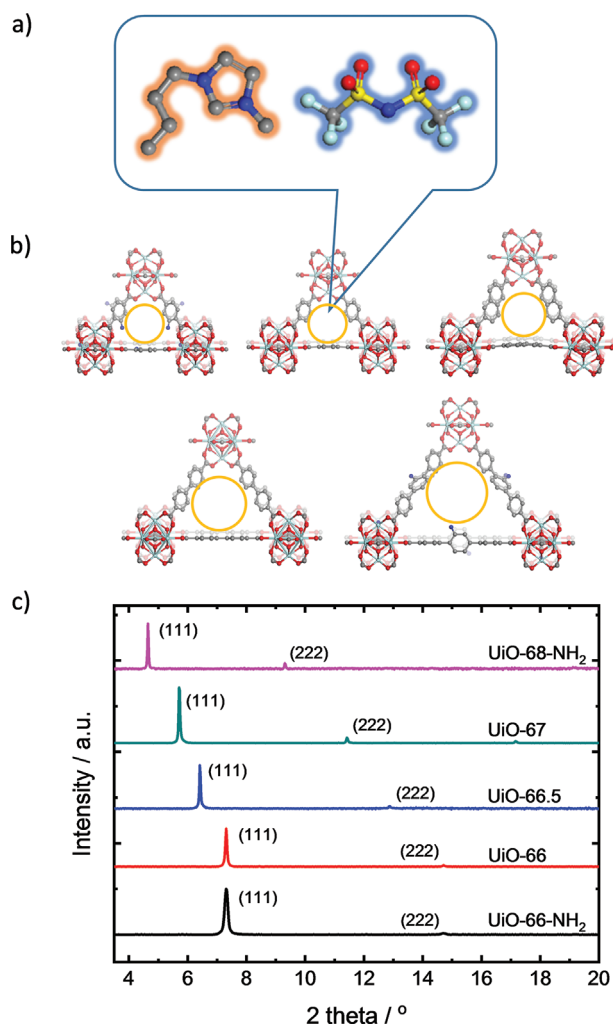


Figure 1. a) Schematic illustration of IL of type [BMIM][TFSI]. b) Structures of the Zr-based MOFs: UiO-66, UiO-66-NH₂, UiO-66.5 (also referred to as DUT-52), UiO-67 and UiO-68-NH₂ (from top-left to bottom-right). The color code for the atoms is C in gray, N in blue, O in red, F in cyan/light-blue (only in the IL), S in yellow, and Zr in cyan (only in MOF). H is not shown. The orange circles represent the pore openings, with diameters of 0.53, 0.55, 0.64, 0.83, and 1.07 nm, respectively, see Figure S13, Supporting Information. c) Out-of-plane XRD data of the MOF films. The comparison of each MOF with the targeted structure is shown in Figure S2, Supporting Information.

the formation of charge-neutral Li-anion complexes.^[10] So far, the impact of the pore size on the IL conduction in nanoporous material has not yet been explored.

Here, in order to explore the influence of the pore size on the mobility of ILs in the nanopores of MOFs, we measure the conductivity and mobility of ILs in a series of Zr-based MOF films with the same topology but different pore sizes. The MOF structures are UiO-66,^[12] UiO-66-NH₂,^[13] UiO-66.5 (here termed for consistent labeling, also referred to as DUT-52 or Zr-NDC),^[14] UiO-67^[15] and UiO-68-NH₂^[16] (UiO stands for Universitetet I Oslo). The MOF films have rather rigid, face-centered cubic crystal structures with isotropic 3D pore systems^[17] connected by pore windows of aperture sizes of 0.53, 0.55, 0.64, 0.83, and 1.07 nm, respectively, see Figure 1 and Figure S13, Supporting

Information. Different amounts of IL of type 1-butyl-3-methylimidazolium bis(trifluoromethylsulfonyl)imide, referred to as [BMIM][TFSI], are embedded in the MOF pores. (Please note, TFSA and NTF₂ are also popular terms for the anion.) The experimental data based on EIS as well as the theoretical data based on molecular dynamics simulations show that the pore size has a severe impact on the ion mobility. In pores larger than a critical diameter, which approximately equals the diameter of the IL ion pair, the drift of the cations and anions in opposite directions is barely hindered and the IL conductivity is only slightly affected by the IL filling in the MOF pores. For MOF pores smaller than the critical diameter, the situation changes drastically. The movement of the cations and anions in opposite directions along the electric field is severely hindered by the pore apertures. While mutual friction is small at low IL loadings in the pores, the ILs mutually hinder the passage of the pore aperture at high IL loadings. This results in a pore blocking by the IL and a bunching of the ions, causing a collapse of the ionic conduction. The study shows for the first time that the pore aperture size must be larger than a critical diameter, here the diameter of an IL-cation-anion-dimer, for fast ion conduction.

2. Results and Discussion

The host MOF structures have the same topology and same metal nodes but different linker molecules, changing the size of the pore body and pore aperture. The MOF films are prepared on the substrates with the deposited interdigitated gold electrodes, see Experimental Section. The MOF films are UiO-66, UiO-66-NH₂, UiO-66.5 (also referred to as DUT-52), UiO-67, and UiO-68-NH₂. The X-ray diffractograms (XRDs, Figure 1) show that all five MOF films have the targeted structure and are grown in the (111) orientation on the substrate. The scanning electron microscopy (SEM) images show that the MOF films have a homogenous morphology, composed of many crystallites, in Figure S1, Supporting Information. The thicknesses of the MOF films were estimated from the images of the broken samples as: 0.37 μm for UiO-66, 0.44 μm for UiO-66-NH₂, 0.46 μm for UiO-66.5, 0.3 μm for UiO-67 and 0.72 μm for UiO-68-NH₂. Please note, that we failed to prepare a highly crystalline, homogenous film of UiO-68 structure, most likely caused by the very limited solubility of the linker molecule. Instead, UiO-68-NH₂ MOF films with high quality were prepared. In the simulations, both MOF films, UiO-68 and UiO-68-NH₂, are discussed and compared.

The MOF-samples were loaded with IL with different pore fillings, which are 15%, 50%, 80%, 95%, and 100%, see experimental section. The ionic conductivity of IL inside the MOF pores was measured via EIS at room temperature. The UiO host MOFs are not electric conducting, so the recorded current and conductance can be solely attributed to the IL in the pores. Typical Nyquist plots of UiO-66 and UiO-67 with different IL pore fillings are shown in Figure 2. The Nyquist plots of the other samples are shown in Figures S3–S5, Supporting Information. The equivalent circuit for the ionic conduction in the MOF films, see Figure 2b, also referred to as (R-CPE_{dl})||CPE_{geo} circuit,^[18] is used for the analysis of the impedance data, to determine the ohmic resistance of the electrolyte R_{electrolyte}. From the ohmic electrolyte resistance, the conductivity of the IL@MOF samples was obtained.

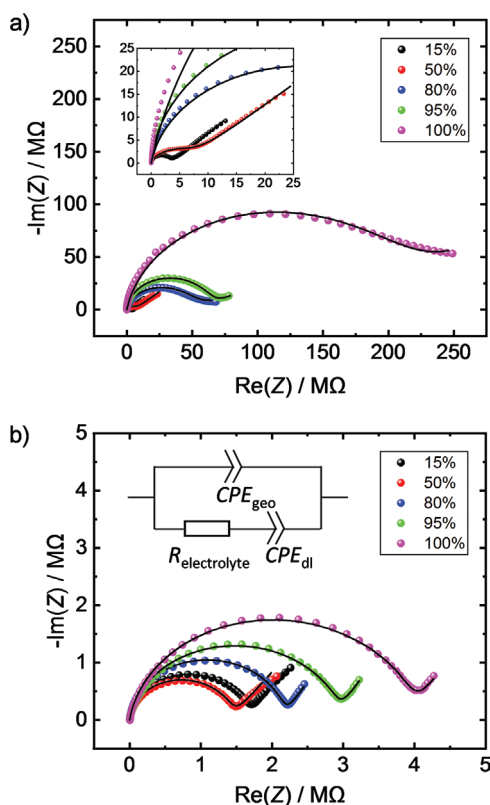


Figure 2. Nyquist plots of the impedance of IL in UiO-66 (a) and UiO-67 (b) MOF films. The degree of IL filling is given in the legends. The inset in (a) shows a zoom-in. The frequency range is 5 MHz (at low impedance) to 0.5 Hz (a) and 10 Hz (b). The colored spheres are the recorded data and the black lines are the fits with the equivalent circuit. The $(R-CPE_{dl})||CPE_{geo}$ equivalent circuit for the ionic conduction in MOFs between two gold electrodes is sketched in the inset in (b).

The conductivity of the IL in the different MOF films versus the IL pore filling is shown in **Figure 3**. For large pore MOFs, only a small loading dependence of the IL conductivity can be found. In detail, the conductivity decreases by a factor of 2 and 3, respectively, for UiO-68-NH₂ and UiO-67. On the other hand, for small pore apertures, like UiO-66 and UiO-66.5, the conductivity drops by ≈ 2 orders of magnitude when increasing the IL pore filling from 15% to 100%.

The data also show that the IL conductivity increases with increasing MOF pore size. A plot of the conductivity versus pore aperture size is shown in **Figure 4a**. While the IL conductivity increases tremendously when increasing the pore aperture from 0.53 to 0.83 nm, only a small conduction increase is observed increasing the pore aperture from 0.83 to 1.07 nm. The data (Figures 3 and) show also no significant difference between UiO-66 and UiO-66-NH₂, indicating that the IL mobility is not affected by the amino groups in the MOF.

For comparing the loading dependence of the conductivity, the ratios of the conductivity at low loading (i.e., 15% pore filling) and maximum loading (i.e., 100% pore filling) are shown in **Figure 4b**. In the plot, 2 regimes can be seen: a strong loading dependence at small MOF pore apertures and a minor loading dependence at large apertures. The transition is ≈ 0.7 – 0.8 nm, which is close to the size of one [BMIM][TFSI]

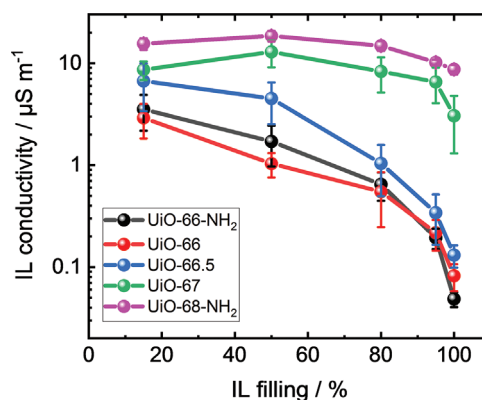


Figure 3. IL conductivity in the different UiO-MOF-hosts with different IL fillings. At each IL filling, the average of five measurements and the standard deviation as error bar are shown. The MOF structures are labeled in the legend.

ion pair, which has a diameter of 0.79 nm.^[19] Although the pore apertures are more triangular than perfectly circular and the cation-anion pair are not perfectly spherical, we believe the simplified relation helps in providing a better understanding.

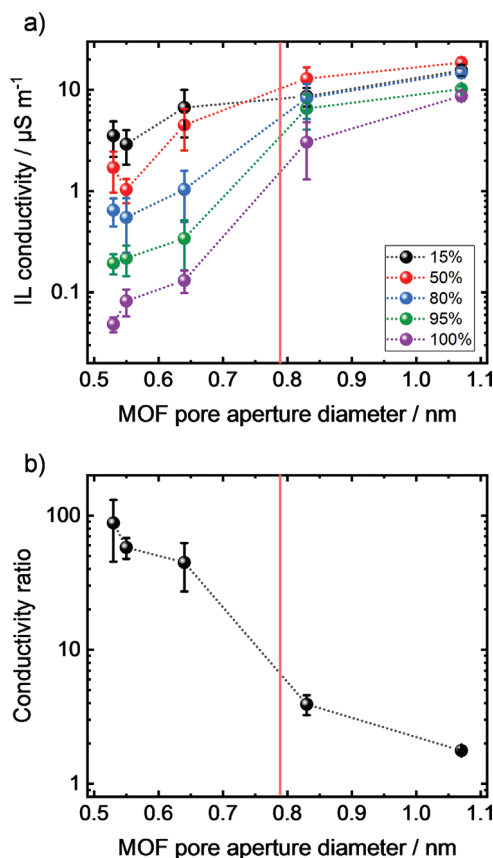


Figure 4. a) IL conductivity at different pore fillings versus the pore aperture size of the different MOFs. The vertical red lines label the diameter of one [BMIM][TFSI] ion pair.^[19] b) Conductivity ratios of IL in the MOFs with different pore aperture sizes. The conductivity ratio is the conductivity at low loading (i.e., 15%) versus at full loading.

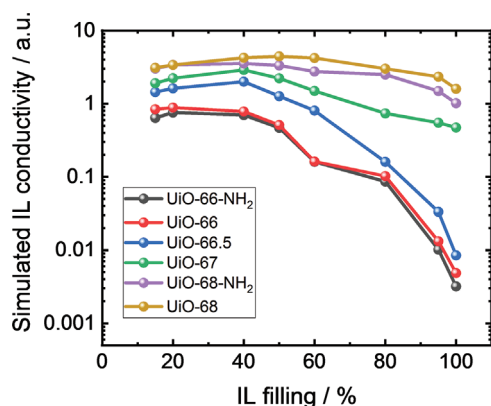


Figure 5. IL conductivity was calculated from MD simulations for [BMIM] [TFSI] in the host MOFs under various IL loadings. The MOF structures are labeled in the legend.

For a deeper understanding of the experimental data, the vehicular conduction of the anions and cations was investigated by molecular dynamics (MD) simulations. For the MD simulations, the same simulation protocol as in our previous work was used.^[10] As host MOFs, in addition to the MOFs used in the experiments, i.e., UiO-66, UiO-66-NH₂, UiO-66.5, UiO-67, and UiO-68-NH₂, the IL transport in UiO-68 was simulated. A defect-free lattice with uniform pores and pore windows was used in the simulations, in line with the experimental data, where a high crystallinity and no indication for a significant defect density were found. Consistent with the experimental setup, where the UiO MOF films are deposited on a substrate with the interdigitated electrodes and grew in the [111] direction perpendicular to the surface, the electric field is aligned along the [110] direction, which is perpendicular to [111]. For the IL transport in [110] direction of the UiO-MOF, the ions have to pass the pore windows in either [100] or [010] direction, thus branching or bifurcating the ion flow in adjacent MOF pores.

The conductivity of the IL in the different host MOFs is shown in **Figure 5**. The simulation results show very good agreement with the experimental data: 1) Comparing the values between the different hosts shows that the conductivity increases with increasing pore size. At small loadings, the difference between the smallest and largest pores is slightly less than one order of magnitude. 2) The dependence of the conductivity on the pore filling changes with the pore size. While there is only a slight loading dependence for large pores with a slight maximum at medium loadings, the conductivity changes by about two orders of magnitude for the small pore MOFs, i.e., UiO-66 and UiO-66.5. 3) No significant differences between the MOFs with and without amino groups, i.e., UiO-66 and UiO-66-NH₂ as well as UiO-68 and UiO-68-NH₂, were found. 4) The concentration dependences of the IL conductivity in the individual MOFs show very similar behavior. For example, both, the simulation and the experimental data for UiO-67 show that the conductivity increases when increasing the pore filling at low loadings, where the maximum is reached at about half the maximum pore filling. When further filling the pores until the maximum IL filling is reached, the conductivity monotonically decreases by about three quarters (i.e., 79% in the experiment and 77% in the simulation). A detailed inspection shows

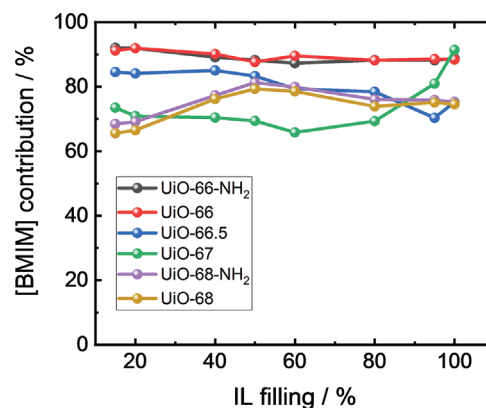


Figure 6. [BMIM] contribution in the IL conductivity calculated from MD under various IL loadings. The MOF structures are labeled in the legend.

a small difference in the course of the conduction decrease between 50% and 100% loading.) We like to stress that all these agreements with the experimental data were obtained without adapting the parameters in the MD simulations. The IL mobilities calculated under various IL fillings are shown in Figure S12, Supporting Information.

To get further insights in the conduction processes, we analyze the MD data in detail. Generally, the MD data show that the cations are significantly more mobile than the anions and contribute the majority to the IL conductivity, **Figure 6**. The mobility of [BMIM] is roughly four times larger than of [TFSI]. Particularly, for UiO-66 and UiO-67 with high IL-loading (where the MOF pores are blocked, see below), the [BMIM] contribution is increased due to a less rigid molecular structure than [TFSI]. While the mobility of the cations and anions in a bulk liquid are similar, see ref. [20] or Figure S18, Supporting Information, in ref. [11a], the mobility of the nanoconfined cations is significantly larger than the nanoconfined anion mobility. This is caused by the rigid anion structure which hinders fast motion in the framework, while the cation is more flexible enabling fast motion. Due to the small pore windows, the discrimination of the molecules in the pore center and close to the pore wall is not possible and a correlation with their mobility, see, e.g., ref., [21] was not performed.

For the small pore MOFs, i.e., UiO-66, UiO-66-NH₂, and UiO-66.5, snapshots of the ions in the pores and the ion trajectories are shown in **Figure 7** and Figure S9a, Supporting Information. The data show that at small IL loadings, the ions drift relatively unhindered through the pore space. The traveled-distance-versus-time diagrams show continuous motion as a linear transport of the ions along the electric field. There, the ion mobility at low loadings is significantly larger in UiO-66.5 than in UiO-66, due to the larger pores. At high loadings, the IL mobility is decreased tremendously. The trajectories show plateaus where the ions are immobile. The mobility drop, and thus the conduction collapse, is induced by the limiting pore windows which prevent the simultaneous passage of the cations and anions in opposite directions, see Figure 7a,b. This results in a mutual pore blocking. The pore blockage further leads to the accumulation and bunching of IL. In the event of IL accumulation and bunching, the van der Waals interaction contributes of roughly

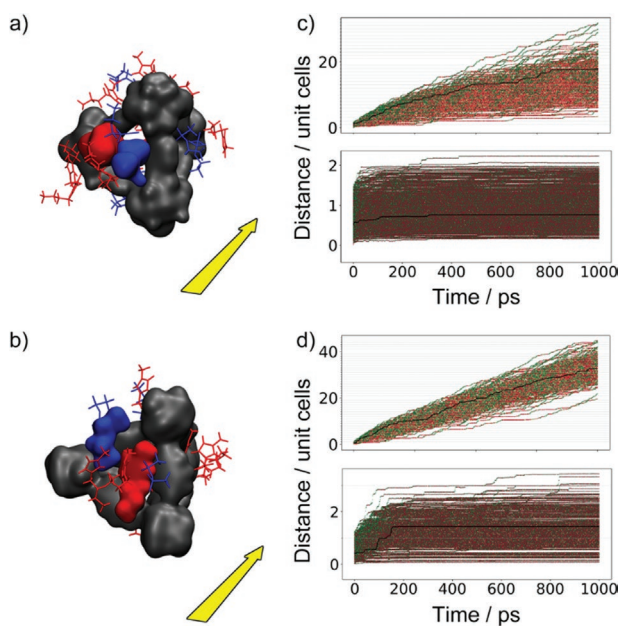


Figure 7. Snapshots of IL in a) UiO-66 and b) UiO-66.5 at 100% IL loading. The [BMIM] cations are depicted in red, [TFSI] anions in blue and the MOFs are shown in grey. The electric field in [110] direction is sketched by the yellow arrows. The MOF as well as one pair of cation and anion at the pore aperture are marked by the corresponding van der Waals surface. Ion trajectories as “traffic maps” of [BMIM] in a 1ns-time window for c) UiO-66 and d) UiO-66.5. The traveled distance in [110] direction is shown. The green color indicates fast motion, red color indicates stagnation. The black line corresponds to a typical trajectory of a single tracer ion. The loading is 50% for the upper plots and 100% for the lower plots.

73% in the overall potential among the cation and anion pairs. The Movies S1a–c (see supporting information) from the MD simulations vividly illustrate the distinctive IL pore blocking in these MOFs. A detailed inspection shows for small pore UiO MOFs, the IL conductivity in the [100] and [010] directions are identical. The IL pore blocking gradually starts at loadings of 40%–60%. The second decline in mobility is observed at $\approx 80\%$ loading. A similar conduction collapse and IL bunching was also found in MOFs with HKUST-1 structure.^[11a] However, the bunching in UiO-66 and UiO-66.5 MOFs occurs at a much lower IL loadings compared to HKUST-1 and the transition of the pore blocking is much milder, i.e., the mobility decreases relatively homogeneously by increasing the pore filling.

Referring to the analogy of traffic jams^[22] for the formation of pore blocking and IL bunching helps to understand the mobility collapse during the (ion) vehicular transport. The bottlenecks in the MOF are the pore windows, which have opening sizes similar to the size of the vehicle, i.e., the IL molecules. For the case of rare occurrence of bottlenecks in a high-density traffic flow, as in HKUST-1, whose pore size is large with many embedded ILs but a limited pore window, the phase transition from a free traffic flow to a traffic jam occurs abruptly. On the other hand, when the density of bottlenecks is larger, as for UiO-66 and UiO-66.5 MOFs with much smaller pore body sizes than HKUST-1, the frequent transient blockage at each single pore aperture affects the neighboring pores and quickly grows into a global bunching layer. There, a mild transition

occurs from free traffic flow to a traffic jam with respect to the increasing IL loading.

The results of the MD simulations of the IL conduction in large pore MOFs, i.e., UiO-67 and UiO-68-NH₂, are shown in Figure 8. The snapshots show the pore apertures are large enough to allow the simultaneous passage of a cation and an anion through the pore window. As a result, the mutual pore blocking by the ions is much suppressed for the large-pore MOFs.

A detailed inspection for UiO-67 shows that the trajectories also have short plateaus indicating a transient pore blockage. However, compared to the small pore MOFs, these plateaus are much reduced. The ion immobilizations are caused by the pore blocking of many (usually 2 or 3) cations and anions simultaneously via an unstable and evanescent formation of amorphous ion clusters. Moreover, the IL motion shows a strong bifurcating behavior in the [100] and [010] directions. At high IL loadings, one of the major ion transport channels, in either [100] or [010], is blocked by the ions whereas the pore channel in the alternative direction is free. The ions bypass the blocked pore windows so that a global IL bunching and a conduction collapse is prevented. The partial pore blockage is indicated by the paths of tracer ions, in Figure 8. The motion speed profiles in Figure S10, Supporting Information, show an asymmetric shape, also indicating the partial pore blockage. Among a series of MD simulations, the single-channel-pore-blocking occurs either in [100] or [010] direction with equal probabilities, shown

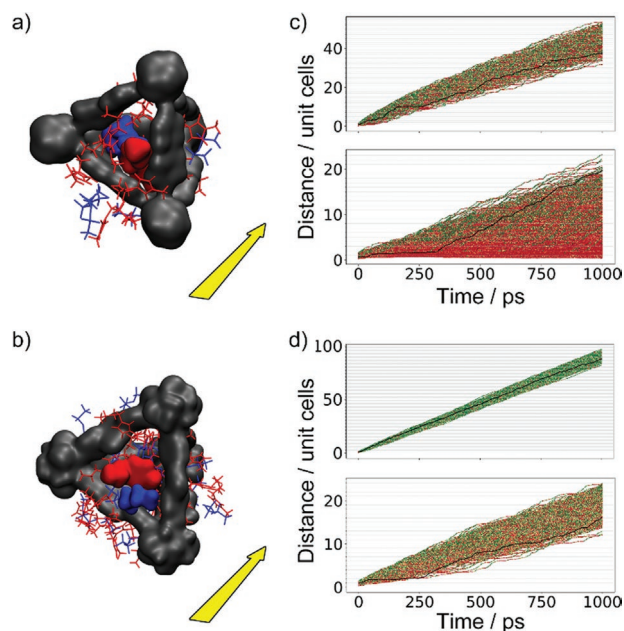


Figure 8. Snapshots of IL in a) UiO-67 and b) UiO-68-NH₂ at 100% IL loading. The [BMIM] cations are depicted in red, [TFSI] anions in blue and the MOFs are shown in grey. The electric field in [110] direction is sketched by the yellow arrows. The MOF as well as one pair of cation and anion at the pore aperture are marked by the corresponding van der Waals surface. Ion trajectories as “traffic maps” of [BMIM] in a 1ns-time window for c) UiO-67 and d) UiO-68-NH₂. The traveled distance in [110] direction is shown. The green color indicates fast motion, red color indicates stagnation. The black line corresponds to a typical trajectory of a single tracer ion. The loading is 50% for the upper plots and 100% for the lower plots. The plot for UiO-68 is shown in Figure S9b, Supporting Information.

in Figures S7d and S8, Supporting Information. In UiO-68 MOFs with even larger pores than UiO-67, such a bifurcation cannot be observed, in Figure S7e–f, Supporting Information. A comprehensive comparison for the bifurcating conductivity in all UiO MOFs is shown in Figure S7, Supporting Information. The motion speed profiles of the IL transport are shown in Figure S11, Supporting Information.

A detailed inspection of the high-loading-UiO-68 data reveals short plateaus in the single ion trajectories. Such short-termed events are observed in the MD simulations where many anions and cations mutually block the passage through the pore window. However, the stand-off situation among the ions is very transient due to the large pore size, and the formation of local traffic jams does not lead to a global immobilization.

In the MD simulations (using the OPLS-AA model^[23]), the amino groups at the UiO MOFs marginally hinder the IL motion. The conductivity of IL in UiO-66-NH₂ and in UiO-68-NH₂ are somewhat smaller than in UiO-66 and UiO-68, respectively, most likely caused by the slightly smaller pore aperture. However, the difference is very small, consistent with the experimental observations. The mobility of the IL in UiO-66-NH₂ and UiO-68-NH₂ as well as its concentration dependence is very similar to its non-amino counterparts of UiO-66 and UiO-68, respectively, see Figures 5,6 or S12, Supporting Information.

It was shown in different studies that the capacitance of the confined IL substantially increases for small, sub-nanometer-sized pores.^[24] Thus we believe pores which are barely larger than the diameter of the IL dimer (from UiO-67 onwards) show the best trade-off between high ion mobility in large pores for fast charging and discharging processes and a high-capacitance in small pores.

3. Conclusion

The mobility of ionic liquids of type [BMIM][TFSI] in the nanopores of the isorecticular UiO-MOF-series with pore aperture diameters from 0.53 nm to 1.08 nm is explored with a combined experimental and theoretical approach. The experimental data, based on EIS using thin films with various IL loadings, show that the pore diameter has a significant impact on the conduction. Molecular dynamics simulations are in agreement with the experiments, providing further insights in the conduction mechanism. The data show that, at low loadings, the IL conduction is barely hindered by the framework or other ions. The low-loading conductivity increases by a factor of 5 when increasing the pore size. For high IL loadings in the pores, the conduction mechanism is governed by the pore size. For the large pore MOF UiO-68, the ions are barely hindered, the ions drift along the electric field and the conduction shows only a very small concentration dependence, where the conductivity drops by a factor of 2, comparing low and full loading. For small pore MOFs of type UiO-66, the pore windows hinder the mutual passage of anions and cations along the electric field, in opposite directions. A strong loading dependence of the conductivity is found, where the conduction drops by two orders of magnitude. Remarkably, the cutoff between highly mobile and immobile IL in the pores occurs at a pore aperture between

0.64 and 0.83 nm, indicating that the diameter of the IL pair (0.79 nm) is a good measure for the cutoff.

We believe that the provided insight will contribute to the further development of IL-based supercapacitors, based on MOFs^[8b] but also based on other nanoporous materials.^[25] By further systematic optimization of the pore structure and of the ILs, the IL mobility will be further improved, allowing ultra-fast, high-capacitance IL-based-supercapacitors.

4. Experimental Section

MOF Synthesis and IL Loading: The MOF thin films were prepared on glass substrates with interdigitated gold electrodes (IDEs) using the vapor-assisted conversion (VAC) method.^[26] In detail, for the film formation using VAC, a glass bottle (250 mL) with a polybutylene terephthalate (PBT) cap equipped with a Teflon seal was used. Raschig-rings (10 mm × 10 mm, soda-lime glass) were put on the bottom part of the bottle to obtain an elevated flat platform for the substrate. A mixture of DMF (4.2 mL) and acetic acid (0.8 mL) was filled into the bottle. A substrate with interdigitated gold electrodes was placed on top of the Raschig-rings and fully coated with a drop of the freshly prepared MOF precursor solution. For the precursor solution, ZrOCl₂·8H₂O was dissolved in DMF. The linker and acetic acid were added to this solution. The bottle was heated to 120 °C and kept for 3 h in the oven. After cooling down, the sample was dried under reduced pressure (1 × 10⁻² bar) overnight.

The IL loading of the MOFs was performed following a previously optimized method.^[11] The samples were immersed in IL/acetonitrile solutions with IL-ratios of 15%, 50%, 80%, 95%, and 100%. After an immersion for 20 min at room temperature (298 K), the samples were briefly rinsed with acetonitrile to remove IL from the outer sample surface, this means to remove excess ILs outside the MOF pores, as previously explored and optimized.^[11b] Then, the samples were dried in a flow of pure nitrogen, removing acetonitrile, which is volatile at room temperature, from the pores. Previously, it was found that the IL loading in the MOF pores is essentially proportional to the IL concentration in the IL/acetonitrile solution.^[10,11]

The X-ray diffractograms were measured in out-of-plane geometry using a Bruker D8-Advance diffractometer equipped with a position-sensitive detector in Θ – Θ geometry. A Cu-anode with a wavelength of $\lambda = 0.154$ nm was used. The scanning electron microscope (SEM) measurements were performed on a TESCAN VEGA3. In order to avoid charging effects, all samples were coated with a 3–4 nm thick platinum film before recording the SEM images.

Measurement of ionic conduction: The electrochemical impedance spectra were measured with a Zurich Instruments MFIA Impedance Analyzer for a frequency range of 5 MHz–0.5 Hz at room temperature. The samples were placed in a home-made Teflon cell where the interdigitated gold electrodes were contacted in a two-probe way. The applied AC voltage is 300 mV, this means the electric field between two (interdigitated) electrodes is ≈ 0.03 V μm^{-1} . The cell was purged with pure nitrogen with a flow rate of roughly 100 mL min⁻¹. The impedance data were recorded from three samples of each MOF structure. The IL concentration was varied in five consecutive cycles, first 15%, then 50%, 80%, 95%, and finally 100% IL pore filling. The average values with the standard deviation as error bars are shown.

Molecular Dynamics Simulation: The all-atom MD simulations were carried out for the IL@MOF systems. The UFF4MOF force field is used for the MOF^[27] and the force field for IL is an established ab initio derivation, which was compatible with OPLS-AA.^[10,28] The force field parametrization for the flexible MOF structure is automated by the LAMMPS-interface,^[27] and the partial charges on the MOF is assigned by the eGULP package via the charge equilibration (QEq) method.^[29] The MD simulations are performed using the LAMMPS package.^[30] The simulation timestep is set to $\tau = 0.25$ fs and the Nose-Hoover thermostat^[31] and Nose-Hoover-Andersen barostat^[32] are used to

Table 1. The numbers of [BMIM][TFSI] IL pairs per MOF unit cell at maximum pore filling for the different MOFs.

| | UiO-66-NH ₂ | UiO-66 | UiO-66.5 | UiO-67 | UiO-68-NH ₂ | UiO-68 |
|---|------------------------|--------|----------|--------|------------------------|--------|
| IL pairs per MOF unit cell for maximum IL filling | 9.97 | 10.8 | 17.5 | 32.2 | 62.1 | 67.8 |

model NPT conditions at ambient conditions, pressure $p = 1$ atm and temperature $T = 300$ K. The filling calculation of IL in the MOF is based on van-der-Waals volumes of the MOF pores (i.e., the void volume in the MOF) and of the IL volume,^[33] consistent with the method used in our previous work.^[10,11] The maximum numbers of IL pairs per MOF unit cell resulting in maximum (i.e., 100%) pore filling are given in **Table 1**. The IL filling levels (see Figures 5,6,7,8 and SI, Supporting Information) were calculated by the ratio of the amount of IL pairs per unit cell and the maximum IL filling.

The initial molecular configuration consists of a $4 \times 4 \times 4$ supercell for UiO-66 and UiO-66-NH₂, $3 \times 3 \times 3$ for UiO-66.5 and UiO-67, and $2 \times 2 \times 2$ for UiO-68 and UiO-68-NH₂. The IL molecules are embedded in the MOF with the PACKmol software.^[28] For each IL loading, the simulation protocol consists of an energy minimization using the conjugate gradient method,^[34] followed by a 1 ns relaxation without an external electric field, and a 10 ns simulation after the electric field is switched on. The direction of the electric field is [110], and the IL mobilities were calculated in separate [110], [100], and [010] directions. Due to the limited timescales of MD simulation and the small-pore-constrained slow IL motion, the MD simulations are performed with a strong electric field of $E = 5, 10, \text{ and } 20 \text{ V nm}^{-1}$. In particular, for small pore UiO MOFs as UiO-66-NH₂ and UiO-66, an excessively strong external electric field of 20 V nm^{-1} is required, as ILs possess low mobilities in the pores, shown in Movie S1a, Supporting Information. (Please note, the electric field in the experiments is $0.03 \text{ V } \mu\text{m}^{-1}$.) As the investigated electric fields show similar behaviors, the results corresponding to $E = 20 \text{ V nm}^{-1}$ is incorporated in the manuscript. Consistent with our previous works,^[10,11] the mobility Λ_m of the IL has been derived from the drift velocity kinetically as $\Lambda_m = E^{-1} F \sum_i (q_i \langle \nu_i \rangle)$, where the i -th component corresponds to [BMIM] and [TFSI] respectively. q corresponds to the charge of the ion, ν is the drift velocity, and F is the Faraday constant.

Supporting Information

Supporting Information is available from the Wiley Online Library or from the author.

Acknowledgements

Z.Z. and M.L. contributed equally to this work. Z.Z., C.L., W.W. and L.H. acknowledge funding by the Deutsche Forschungsgemeinschaft (DFG, via SPP 1928 COORNETS and via HE 7036/5 and WE1863/37-1) and by China Scholarship Council (CSC). M.L., W.W. acknowledge the funding support by the DFG Excellence Cluster "3D Matter Made to Order" (3DMM2O, EXS 2082).

Open Access funding enabled and organized by Projekt DEAL.

Conflict of Interest

The authors declare no conflict of interest.

Data Availability Statement

The data that support the findings of this study are available from the corresponding author upon reasonable request.

Keywords

ionic conduction, ionic liquids, metal-organic frameworks, nanoconfinement, pore size

Received: January 27, 2022

Revised: April 5, 2022

Published online:

- a) J. S. Wilkes, *Green Chem.* **2002**, *4*, 73; b) S. A. Forsyth, J. M. Pringle, D. R. MacFarlane, *Aust. J. Chem.* **2004**, *57*, 113; c) D. R. MacFarlane, M. Kar, J. M. Pringle, *Fundamentals of Ionic Liquids: From Chemistry to Applications*, John Wiley & Sons, Weinheim **2017**.
- a) Q. Zhu, Y. Song, X. F. Zhu, X. L. Wang, *J. Electroanal. Chem.* **2007**, *601*, 229; b) M. Chai, Y. D. Jin, S. H. Fang, L. Yang, S. Hirano, K. Tachibana, *J. Power Sources* **2012**, *216*, 323; c) L. P. Yu, G. Z. Chen, *Front. Chem.* **2019**, *7*, 15; d) H. Z. Niu, L. Wang, P. Guan, N. Zhang, C. R. Yan, M. L. Ding, X. L. Guo, T. T. Huang, X. L. Hu, *J. Energy Storage* **2021**, *40*, 102659.
- a) C. X. Peng, Z. B. Wen, Y. Qin, L. Schmidt-Mende, C. Z. Li, S. H. Yang, D. L. Shi, J. H. Yang, *ChemSusChem* **2014**, *7*, 777; b) F. W. Richey, C. Tran, V. Kalra, Y. A. Elabd, *J. Phys. Chem. C* **2014**, *118*, 21846; c) K. Fujie, H. Kitagawa, *Coord. Chem. Rev.* **2016**, *307*, 382.
- a) N. N. Rajput, J. Monk, F. R. Hung, *J. Phys. Chem. C* **2012**, *116*, 14504; b) M. P. Singh, R. K. Singh, S. Chandra, *Prog. Mater. Sci.* **2014**, *64*, 73; c) S. G. Zhang, J. H. Zhang, Y. Zhang, Y. Q. Deng, *Chem. Rev.* **2017**, *117*, 6755.
- C. Young, J. Lin, J. Wang, B. Ding, X. Zhang, S. M. Alshehri, T. Ahamad, R. R. Salunkhe, S. A. Hossain, J. H. Khan, *Chem. - Eur. J.* **2018**, *24*, 6127.
- a) M. Biagooi, S. N. Oskoe, *Sci. Rep.* **2020**, *10*, 6533; b) J. M. Otero-Mato, H. Montes-Campos, O. Cabeza, L. J. Gallego, L. M. Varela, *J. Mol. Liq.* **2020**, *320*, 114446.
- a) S. Kaskel, *The Chemistry of Metal-Organic Frameworks, 2 Volume Set: Synthesis, Characterization, and Applications*, John Wiley & Sons, Weinheim **2016**, Vol. 1; b) I. Stassen, N. Burtch, A. Talin, P. Falcaro, M. Allendorf, R. Ameloot, *Chem. Soc. Rev.* **2017**, *46*, 3185; c) S. Yuan, L. Feng, K. C. Wang, J. D. Pang, M. Bosch, C. Lollar, Y. J. Sun, J. S. Qin, X. Y. Yang, P. Zhang, Q. Wang, L. F. Zou, Y. M. Zhang, L. L. Zhang, Y. Fang, J. L. Li, H. C. Zhou, *Adv. Mater.* **2018**, *30*, 35.
- a) Z. Q. Wang, R. Tan, H. B. Wang, L. Y. Yang, J. T. Hu, H. B. Chen, F. Pan, *Adv. Mater.* **2018**, *30*, 7; b) Y. Yoshida, H. Kitagawa, *ACS Sustainable Chem. Eng.* **2019**, *7*, 70.
- S. Bi, H. Banda, M. Chen, L. Niu, M. Y. Chen, T. Z. Wu, J. S. Wang, R. X. Wang, J. M. Feng, T. Y. Chen, M. Dinca, A. A. Kornyshev, G. Feng, *Nat. Mater.* **2020**, *19*, 552.
- M. Vazquez, M. Liu, Z. J. Zhang, A. Chandresh, A. B. Kanj, W. Wenzel, L. Heinke, *ACS Appl. Mater. Interfaces* **2021**, *13*, 21166.
- a) A. B. Kanj, R. Verma, M. D. Liu, J. Helfferich, W. Wenzel, L. Heinke, *Nano Lett.* **2019**, *19*, 2114; b) Z. J. Zhang, C. Li, A. Chandresh, L. Heinke, *Ionics* **2022**, *28*, 487.
- M. Kandiah, M. H. Nilsen, S. Usseglio, S. Jakobsen, U. Olsbye, M. Tilset, C. Larabi, E. A. Quadrelli, F. Bonino, K. P. Lillerud, *Chem. Mater.* **2010**, *22*, 6632.
- G. W. Peterson, J. J. Mahle, J. B. DeCoste, W. O. Gordon, J. A. Rossin, *Angew. Chem., Int. Ed.* **2016**, *55*, 6235.
- V. Bon, I. Senkovska, M. S. Weiss, S. Kaskel, *CrystEngComm* **2013**, *15*, 9572.
- S. Chavan, J. G. Vitillo, D. Gianolio, O. Zavorotynska, B. Civalieri, S. Jakobsen, M. H. Nilsen, L. Valenzano, C. Lamberti, K. P. Lillerud, S. Bordiga, *Phys. Chem. Chem. Phys.* **2012**, *14*, 1614.

- [16] A. Schaate, P. Roy, A. Godt, J. Lippke, F. Waltz, M. Wiebcke, P. Behrens, *Chem. - Eur. J.* **2011**, *17*, 6643.
- [17] J. H. Cavka, S. Jakobsen, U. Olsbye, N. Guillou, C. Lamberti, S. Bordiga, K. P. Lillerud, *J. Am. Chem. Soc.* **2008**, *130*, 13850.
- [18] A. Chandresh, Z. J. Zhang, L. Heinke, *Materials* **2021**, *14*, 4352.
- [19] Y. Yokota, T. Harada, K. I. Fukui, *Chem. Commun.* **2010**, *46*, 8627.
- [20] H. Tokuda, K. Hayamizu, K. Ishii, M. Abu Bin Hasan Susan, M. Watanabe, *J. Phys. Chem. B* **2004**, *108*, 16593.
- [21] B. Coasne, L. Viau, A. Vioux, *J. Phys. Chem. Lett.* **2011**, *2*, 1150.
- [22] a) M. Treiber, A. Hennecke, D. Helbing, *Phys. Rev. E* **2000**, *62*, 1805; b) B. S. Kerner, H. Rehborn, R. P. Schafer, S. L. Klenov, J. Palmer, S. Lorkowski, N. Witte, *Physica A* **2013**, *392*, 221.
- [23] K. Shimizu, D. Almantariotis, M. F. C. Gomes, A. A. H. Padua, J. N. C. Lopes, *J. Phys. Chem. B* **2010**, *114*, 3592.
- [24] a) J. Chmiola, G. Yushin, Y. Gogotsi, C. Portet, P. Simon, P. L. Taberna, *Science* **2006**, *313*, 1760; b) C. Largeot, C. Portet, J. Chmiola, P. L. Taberna, Y. Gogotsi, P. Simon, *J. Am. Chem. Soc.* **2008**, *130*, 2730; c) C. Iacob, J. R. Sangoro, W. K. Kipnusu, R. Valiullin, J. Kärgler, F. Kremer, *Soft Matter* **2012**, *8*, 289.
- [25] a) J. Vatamanu, M. Vatamanu, D. Bedrov, *ACS Nano* **2015**, *9*, 5999; b) P. Simon, Y. Gogotsi, *Nat. Mater.* **2020**, *19*, 1151.
- [26] E. Virmani, J. M. Rotter, A. Mähringer, T. Von Zons, A. Godt, T. Bein, S. Wuttke, D. D. Medina, *J. Am. Chem. Soc.* **2018**, *140*, 4812.
- [27] P. G. Boyd, S. M. Moosavi, M. Witman, B. Smit, *J. Phys. Chem. Lett.* **2017**, *8*, 357.
- [28] Z. J. Li, Y. L. Xiao, W. J. Xue, Q. Y. Yang, C. L. Zhong, *J. Phys. Chem. C* **2015**, *119*, 3674.
- [29] A. K. Rappe, W. A. Goddard, *J. Phys. Chem.* **1991**, *95*, 3358.
- [30] S. Plimpton, *J. Comput. Phys.* **1995**, *117*, 1.
- [31] W. G. Hoover, *Phys. Rev. A* **1985**, *31*, 1695.
- [32] H. C. Andersen, *J. Chem. Phys.* **1980**, *72*, 2384.
- [33] Y. H. Zhao, M. H. Abraham, A. M. Zissimos, *J. Org. Chem.* **2003**, *68*, 7368.
- [34] D. Sheppard, R. Terrell, G. Henkelman, *J. Chem. Phys.* **2008**, *128*, 134106.